Investigating the behavior of an expansive soil slope in critical linear infrastructure in China using multi-temporal InSAR

Zhen Jiang[1], Zigui Wu[2], Ziyuan Li[3]*, Jun Hu[3], Yuwei Wu[1], Liye Ou[1] and Tongyuan Zhang[2]

[1]Jiangxi Institute of Land Space Survey and Planning, Nanchang, China, [2]State Grid Ji'an Electric Power Supply Company, Ji'an, China, [3]School of Geosciences and Info-Physics, Central South University, Changsha, China

One of the most significant pieces of linear infrastructure in China is the Middle Route of the South-to-North Water Diversion Project (MR-SNWDP), a large section of which consists of an expansive soil slope (ESS) that threatens the safety of the canal. Here, we prepared 144 Sentinel-1 data from May 2017 to July 2022 to study the behavior of the ESS in the canal section in Huixian City in the MR-SNWDP. Then, the Elastoplastic Deformation model under Wetting and Heating Effects (EDWHE) was employed to accurately characterize the displacement of the ESS. The InSAR results illustrate that the unstable zones tend to be small and are distributed along the canal slope, with the magnitude of deformations generally no more than 20 mm/year. Additionally, their deformation time series generally accumulate exponentially and evolve in a significant pattern of seasonal swelling and shrinkage. We observed that the slope movements significantly accelerated during the period when extreme rainfall occurred around 22 July 2021. Affected by satellite imagery and the geometric structure of the slope, the magnitudes and evolving trends of LOS deformation vary with different aspects of the slope sections. Then, the elastic swelling-shrinkage deformations were derived through the EDWHE model, of which the uplift or settlement was mainly dependent on geological and meteorological conditions. Moreover, the active zone depths of the ESS were retrieved using an InSAR-based lag-time approach and clearly reflected their distribution pattern. In this investigation, the behavior of the ESS in the study area was quantitatively analyzed using InSAR, and the results provide support for designing protective slope treatments and keeping the canal safe in the MR-SNWDP.

1 Introduction

The Middle Route of the South-to-North Water Diversion Project (MR-SNWDP) is an extremely significant infrastructure project in China and is effective at alleviating the imbalance in water distribution between South and North China (Office of the South-to-North Water Diversion Project Construction Committee et al., 2016; Dong et al., 2021). It has a total length of 1,432 km from Danjiangkou Reservoir, Henan, to Beijing and largely consists of excavated and filled slopes. However, 387 km of the MR-SNWDP is well

distributed with destructive expansive soil, posing a significant threat to the safety of the channel slopes (Dai et al., 2021; Dong et al., 2021).

The damage to infrastructure by expansive soil is mainly attributed to its elastic volume swelling/shrinking in response to soil moisture gain/loss (Mitchell, 1980; Ng et al., 2003; Zhan et al., 2007). The soil swells and shrinks repeatedly with wetting-drying cycles, which conforms to elastic behavior (Wang and Wei, 2014; Qi and Vanapalli, 2016; Li et al., 2023), facilitating soil mass softening and then accumulating plasticity. An expansive soil slope (ESS) acts as the down-slope shallow displacement and probably ends up inducing a progressive failure (Ng et al., 2003; Dai et al., 2021). Especially for the MR-SNWDP, which is subject to a monsoon season, expansive soil undergoes coupled swelling and shrinkage in summer that accelerates the process of wetting-drying cycles and thus faces more severe geohazard problems (Yang et al., 2006; Li et al., 2023). Therefore, for the safety of the MR-SNWDP, the characterization of the elastoplastic displacements of an ESS plays a significant role in preventing geohazards. In addition, a better understanding of the swelling and shrinkage dynamics of an ESS can help the design of more effective treatments for unstable slopes (Ting et al., 2018; Cohen-Waeber et al., 2023; Li et al., 2023).

The ground displacements of expansive soil receive contributions from the volume change of soil mass within a certain depth that is generally referred to as the active zone depth (AZD) (Aubeny and Long, 2007; Yue and Veenstra, 2018; Huang et al., 2022). It essentially defines the zone where moisture beneath the ground moves and soil deforms. AZD is a fundamental parameter for foundation design and protective treatment (Zongjun et al., 2006; Yue and Veenstra, 2018; Huang et al., 2022). Given the active zone, we can effectively protect against unstable slopes in the MR-SNWDP.

The Interferometric Synthetic Aperture Radar (InSAR) technique provides us with the ability to approach the demands mentioned previously. InSAR allows the remote imaging of vast earth surfaces at one time with high spatial resolution, after which multitemporal InSAR (MT-InSAR) can observe ground displacements in a magnitude of millimeters. Nowadays, huge archives of SAR data (e.g., Sentinel-1 data or NISAR in the future) make it convenient to characterize more detailed deformation patterns (Zheng et al., 2023). There have been many instances in which MT-InSAR has been successfully used to study the pattern of ground displacements caused by groundwater exploitation, active slow-moving landslides, and some special soil issues (Chaussard et al., 2014; Zhao et al., 2016; Miller et al., 2017; Hu et al., 2020; Lan et al., 2021; Cohen-Waeber et al., 2023; Dong et al., 2023). Furthermore, some publications have investigated the deformation distribution on a section of the MR-SNWDP and studied the destructive behavior of expansive soil––the swelling and shrinkage responsible for wetting and drying (Vallone et al., 2008; Bonì et al., 2018; Özer et al., 2019; Cook, 2023; Xiong et al., 2023).

InSAR time series have demonstrated the advantages of characterizing the downslope displacements of the ESS with seasonal variation (Zhang et al., 2022; Cook, 2023). Some methods, such as using a specific deformation model or independent component analysis, have been employed to investigate the characteristics of ESS movement, and its lagging

effect on soil wetting (and drying) has been further studied (Özer et al., 2019; Cohen-Waeber et al., 2023). Owing to the monsoon season, the expansive soil's expansion and contraction are coupled, resulting in a more complex deformation pattern that has a higher risk of inducing geohazards in the MR-SNWDP. Then, an Elastoplastic Deformation model under Wetting and Heating Effects (EDWHE) is proposed to characterize this deformation pattern of the ESS in the channel head of the MR-SNWDP, and an InSAR-based time-lag approach is developed to retrieve the corresponding slope's AZD (Li et al., 2023). Here, considering the heterogeneity of expansive soil and the different engineering geological setting, we intend to employ the EDWHE model and time-lag approach to explore its spatiotemporal pattern on a larger scale and study the behavior of the ESS further in another section of the MR-SNWDP, i.e., the canal sections in Huixian City, Henan. In addition, with the knowledge that an unusually heavy rainstorm occurred there on 22 July 2021, we try to investigate how the extreme precipitation impacts the ESS displacements.

In this paper, a Sentinel-1 SAR dataset covering the study area, the canal section in Huixian City, is collected, spanning from July 2017 to May 2022, with a total of 144 scenes. The EDWHE model is applied to investigate the deformation pattern of ESS in the study area, in which the by-products, the expansive soil's time delays corresponding to rainfall and temperature, are obtained for analysis and subsequent work. Then, the elastoplastic displacement of the ESS is discussed in detail, and the elastic component is derived from the EDWHE model to explore its characteristics in response to rainfall events and temperature changes. In addition, we employ the time-lag approach to derive the AZD along the canal slope. Our study on the behavior of the ESS in multiple aspects provides support for the prevention of the expansive soil geohazard in the MR-SNWDP.

2 Materials

2.1 Geological setting of the study area

The canal section is located in Huixian City, northern Henan Province, China. It flows through the northeast boundary of the urban area and extends eastward, covering part of the ESS in this section. The canal section in Huixian City is hereafter called CSHC for simplicity. The geographical location and spatial distribution of the canal are shown in Figure 1. The expansive soils in Huixian City are mainly Upper Tertiary littoral lake facies, fluvial lacustrine sedimentary strata, and Quaternary Middle Pleistocene alluvial and diluvial strata (Q2al + pl), including heavy silty loam, silty clay, marl, and clay rock, with weak expansibility (Xu et al., 2019; Zhang et al., 2021). Owing to the specific expansion and contraction of the ESS in the channel, the cracks in the upper zone are fully developed, and the level of soil saturation is high, which seriously weakens the shear strength and causes severe damage to the safety of the ESS (Xu et al., 2019).

Under the influence of expansive soil, there is a high risk of geohazards occurring on the ESS, which would affect the safe operation of the water diversion channel (Li et al., 2023). Therefore, the EDWHE InSAR model is applied in this study to investigate the potential hazards of the expansive soil slope in the
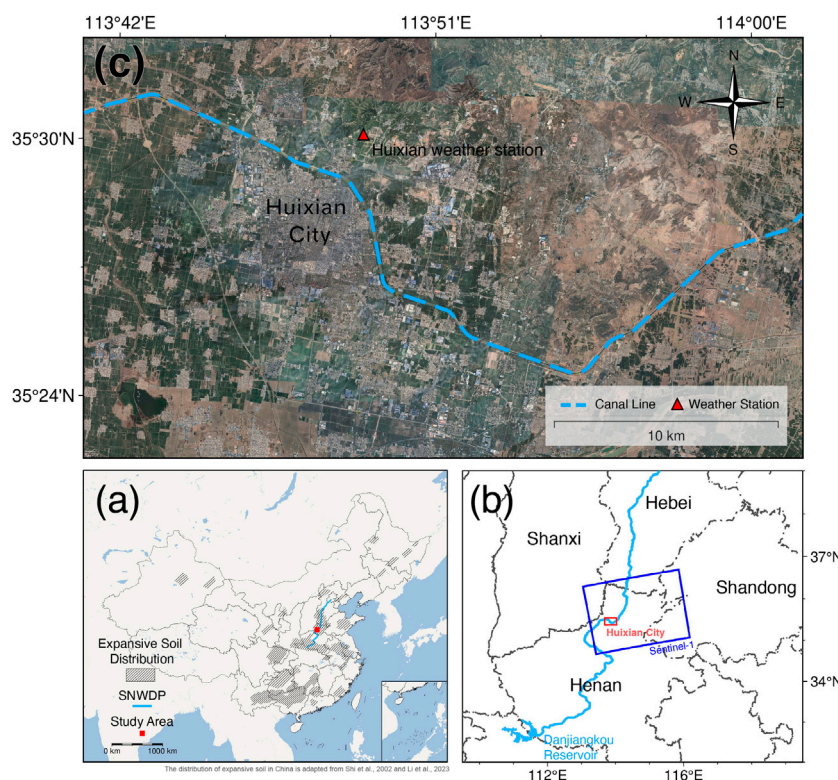
FIGURE 1
Geographical location and spatial distribution of the canal section in Huixian City, Henan, China. **(A)** The location of the study area and the distribution of expansive soil in China (Shi et al., 2002; Li et al., 2023). **(B)** More detailed information about the geographical location of the study area and the footprint of the Sentinel-1 SAR data in path 40 and frame 112. **(C)** Optical image obtained by Google Earth. The dashed blue line delineates the channel.

TABLE 1 Parameters of the Sentinel-1 SAR data used in this study.

Parameters	Description
SAR satellite	Sentinel-1A
Orbit direction	Ascending
Path	42
Frame	112
Number of scenes	144
Time span	July 2017–May 2022

Huixian City channel in the MR-SNWDP and study the dynamics of expansive-soil deformation, providing a better understanding of expansive soil geohazards. Furthermore, the method of retrieving the AZD is used to obtain the active layer of expansive soil in this channel section, providing support for an effective protective measure.

2.2 The dataset

In this study, the Sentinel-1 SAR data of ascending orbit in path 42 and frame 112 were obtained, spanning from July 2017 to May 2022, with 144 scenes, as shown in Figure 1B. The specific parameters of the SAR data used are listed in Table 1. The thresholds of the perpendicular and temporal baselines were set to 200 m and 96 days, respectively, for the construction of the multi-baseline interferometric pairs. To avoid the influence of severe atmospheric and decoherent noise, the interferograms with significantly noisy fringes in the objective region were excluded as much as possible, and finally, a total of 387 high-quality interferometric pairs were obtained. The resulting spatiotemporal baseline network is shown in Figure 2. In addition, to more accurately remove the contribution of the height phase, 30 m Copernicus DEM, derived during the MR-SNWDP construction, was used for differential interferometry.

Before the InSAR analysis using the EDWHE model, it is necessary to collect enough meteorological data, i.e., precipitation and temperature records, as the inputs of the EDWHE model, which can also support the subsequent analysis of the behavior of the ESS. For this reason, the daily rainfall and temperature data from recent years from the weather station in Huixian City were collected, as shown in Figure 3. It should be noted that there was abnormally high rainfall on 22 July 2021, much higher than the daily rainfall peak in previous years (corresponding to the peak in Figure 3).

3 Methodology

In this study, the EDWHE model was applied to investigate the deformation pattern of the ESS in the Huixian City section of the
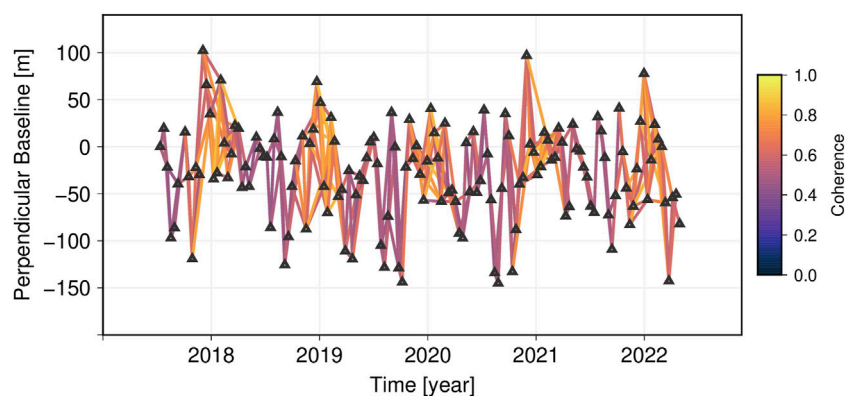
FIGURE 2
Spatiotemporal baseline network, with 200-m and 96-day perpendicular and temporal baseline thresholds, respectively.
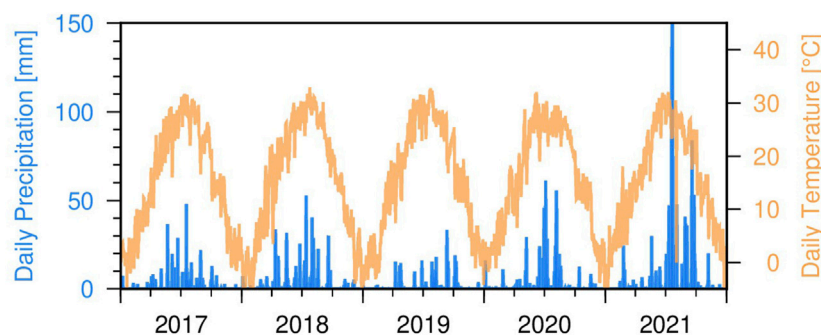

FIGURE 3
Meteorological data from the weather station in Huixian City, which were used to construct the deformation model and for subsequent analysis. The blue bars denote the daily precipitation records and the solid yellow lines indicate the daily temperature records.

MR-SNWDP. The time-lag approach was used to determine the active zone of the expansive soil (Li et al., 2023). The overall flowchart of the study is shown in Figure 4.
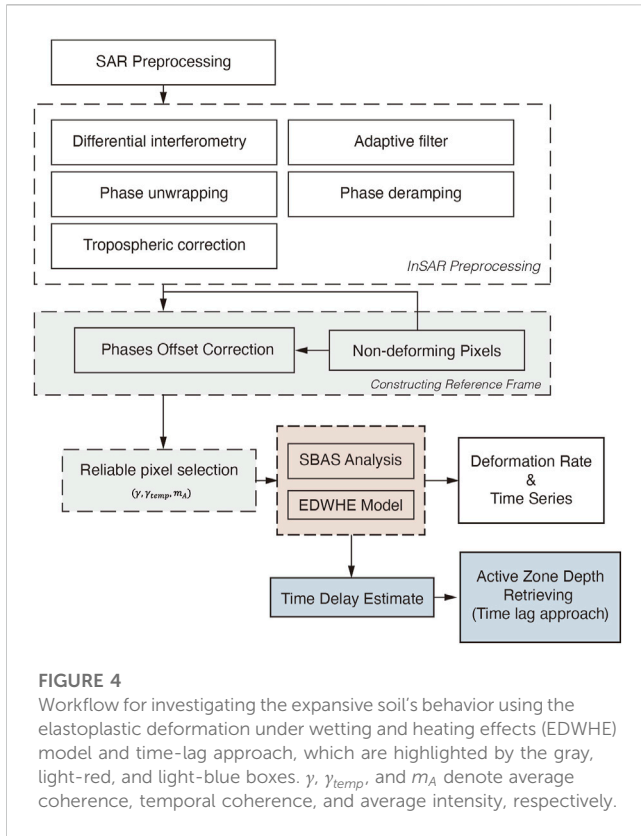
3.1 SAR data preprocessing

SAR data preprocessing, including co-registration, multi-look (4 × 1 in range and azimuth), and interferometry, was first completed using GAMMA software. Then, the adaptive filter and minimum-cost flow (MCF) were separately implemented to suppress the noisy signal and unwrap the phase (Goldstein and Werner, 1998; Costantini and Rosen, 1999). The filtering window should be relatively small to retain the spatial detail as much as possible. After that, phase ramps were removed by fitting the polynomial function before the time-series analysis, and a topographic power-law exponential model was exploited to mitigate the tropospheric disturbance (Bekaert et al., 2015; Li et al., 2019; Liang et al., 2019).

Considering that the research object (the expansive soil slope) is distributed in a pattern of long and narrow strips, which only occupies a small part of the whole image and the coverage area of the SAR data, there are various ground objects and complicated

ground activities possibly affecting deformation interpretation. Therefore, to focus more on the spatial deformation pattern and analysis of the ESS along the channel of the MR-SNWDP, we created a 1 km buffer along both sides of the canal line with the InSAR data to isolate the main region of the channel, as shown in Figure 5.

Here, the strategy of multiple quality measures to select reliable pixels was employed (Yunjun et al., 2019; Li et al., 2023), in which the measures included average coherence γ, temporal coherence γ_{temp}, and average intensity m_A, separately shown in Supplementary Figures S1B–D. When selecting reliable points, the average coherence $\gamma_0 = 0.65$ was initially applied to mask out low-coherence pixels, after which the pixels with low phase closure and faint decoherence were further picked out by $\gamma_{temp,0} = 0.7$ (Yunjun et al., 2019; Li et al., 2023). Then, the average intensity (of the threshold set as 0.02) wass used as a complement to separate the pixels in the water body from the selected pixel subset. The final result is shown in Supplementary Figure S1A. As InSAR is a well-developed technique and has been qualified by a great deal of advanced research, the numerous practices demonstrate that we could calculate a theoretical accuracy of InSAR deformation through the given coherence and the Cramer–Rao bounds (Rodriguez and Martin, 1992; Delbridge et al., 2016; Zheng et al., 2023). The theoretical accuracy of InSAR deformation can be derived

FIGURE 4
Workflow for investigating the expansive soil's behavior using the elastoplastic deformation under wetting and heating effects (EDWHE) model and time-lag approach, which are highlighted by the gray, light-red, and light-blue boxes. γ, γ_{temp}, and m_A denote average coherence, temporal coherence, and average intensity, respectively.

through the given parameters above (multi-look ratio, wavelength, and average coherence) and was 1.8 mm.

Owing to the widespread existence of expansive soil in the study area, its unique expansion and contraction characteristics can increase the difficulty of selecting reference points in constant phase correction, which in turn will offset the derived time series of ESSs (Murray and Lohman, 2018; Jiang and Lohman, 2021; Zebker, 2021; Li et al., 2023). Here, we employed a multi-reference frame to mitigate the influence of the inaccurate selection of a local (single) reference, in the same way as Li et al. (2023). Therefore, we calculated the standard deviation (SD) of the time-series deformation of routine SBAS solution (Supplementary
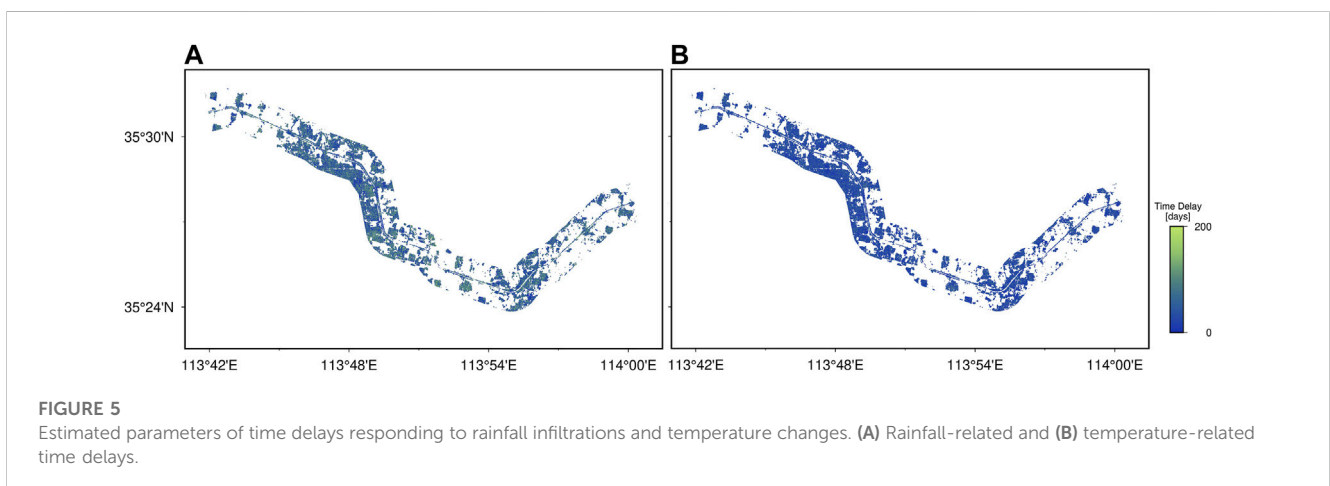
Figure S1A) and identified the reference frame by selecting pixels with an SD of less than 6 mm (Supplementary Figure S1B). Finally, the median phase value of the pixels under the reference frame was calculated and subtracted from each unwrapped interferogram.

3.2 Constructing the EDWHE model

Owing to the expansive soil's characteristics and weather activities, the ESS deforms in a seasonal way that forms a specific elastoplastic behavior. Here, to characterize the deformation of the ESS in the CSHC of the MR-SNWDP, we employed an Elastoplastic Deformation model under Wetting and Heating Effects, referred to as the EDWHE model (Li et al., 2023). In this way, capturing the variations of elastic swelling-shrinkage deformation and the plastic accumulation of the ESS is possible. The EDWHE model is defined as:

$$d_{EDWHE} = d_{pla}(t) + d_{ela}(t)$$
$$= \underbrace{\sum_{k=1}^{n}\alpha_k t^k}_{d_{pla}} + \underbrace{\beta_1 P_e(t-\tau_1) + \beta_2 T_m(t-\tau_2) + c_e}_{d_{ela}} \quad (1)$$

where the first term $d_{pla}(t)$ denotes the plastic deformation of the ESS that is the approximated polynomial function of time t, in which α_k indicates a time-related coefficient; k represents the order of the polynomial function. In this study, we employed $k=4$ to better characterize the non-linear plastic evolution of the ESS. The second term $d_{ela}(t)$ corresponds to elastic deformation relating to efficient rainfall and mean temperature, in which the efficient rainfall $P_e(t-\tau_1) = \sum_{k=1}^{m}\omega^k p(t-\tau_1-k+1)$ can take the persisting effect of previous rainfall infiltration into consideration, where m is taken as 15 days as in Li et al. (2023), $p(t)$ is the rainfall record at time t, and τ_1 is time delays for a deeper layer influence of precipitation infiltration. $T_m(t-\tau_2)$ is the average temperature between two sequential SAR acquisitions, where τ_1 will shift the temperature data to characterize its delay effect. $\beta_i, i=1,2$ can represent the magnitudes of swelling and shrinkage; c_e is the constant offset caused by the first two terms. Afterward, the EDWHE model can be integrated with the phase term of the residual height, $\varphi_{topo}^i = \frac{4\pi B_\perp \Delta h}{\lambda r sin\theta}$, into the frame of SBAS analysis.

FIGURE 5
Estimated parameters of time delays responding to rainfall infiltrations and temperature changes. **(A)** Rainfall-related and **(B)** temperature-related time delays.

Here, the pattern-matching method developed by Li et al. (2023) was used to simultaneously estimate the time delays of precipitation and temperature from the coupled elastic swelling and shrinking. The method employed sum square error as the pattern-matching function to find the best similarities between the estimated elastic deformation $\hat{d}_{ela}(t, \hat{\tau}_1, \hat{\tau}_2)$ and the observable one $d_{ela}(t)$:

$$argmin\, SSE\left(d_{ela}, \hat{d}_{ela}\right) = argmin\sum_{t}^{M}\left(d_{ela}(t) - \hat{d}_{ela}(t, \hat{\tau}_1, \hat{\tau}_2)\right)^2 \quad (2)$$

where $d_{ela}(t)$ is first derived by initially assuming zero-value time delays and solving the EDWHE model. Then, an iterative procedure is performed 2–3 times to acquire more accurate estimates.

3.3 Retrieval of the active zone depth

To estimate the AZD of the ESS on the CSHC, we employed an InSAR-based time-lag approach developed by Li et al. (2023). The inversion of the AZD utilizes the derivation of a one-dimension diffusion equation (Mitchell, 1980), as follows:

$$z = 2\Delta t \sqrt{\alpha \pi n} \quad (3)$$

where z is the depth of the active zone, Δt can be represented by the time delay of rainfall $\hat{\tau}_1$, α is the moisture diffusion coefficient, which is usually determined from field measurements or laboratory data, and n is the frequency of the suction cycle. The last two parameters are unknown.

Given the lack of any accessible ground-based data, we empirically used the upper value $\hat{\alpha} = \frac{10^{-7} m^2}{s}$ in a general range 10^{-9} to $10^{-7} m^2$ to be conservative, as suggested by Tu and Vanapalli (2016). Considering the same climatic zone as in Li et al. (2023), the frequency of the suction cycle $n= 2$ was determined. Hereafter, the AZD of the ESS along the channel could be retrieved.

4 Results and discussion

By solving the EDWHE model and employing the time-lag approach, a series of products within the boundaries of the canal buffer have been derived and are shown in this section. Except for general descriptions of the results, we further investigate the underlying behavior of expansive soil with external meteorological conditions in the CSHC.

4.1 Estimated parameters of the EDWHE model

The time delay parameters are crucial in the EDWHE model, accounting for the delayed swelling and shrinkage caused by rainfall infiltration and temperature changes. First, they are estimated through the pattern-matching method; hence, the EDWHE model can be solved in the linear least-square sense. The estimated time delays after three iterations are shown in Figure 5, which shows that the time delays caused by rainfall infiltration, which are generally greater than 100 days (Figure 5A), are

considerably greater than the temperature-related ones, which are generally close to zero (Figure 5B). In addition, the time delays of rainfall seem to spatially distribute in clusters; therefore, the size may be large or small depending on the ground setting (ground types, geological conditions, etc.). Temperature-induced time delays are spatially uniform due to all their lower values. From the results, we can see that the ESS takes longer to respond to rainfall infiltration but, conversely, responds rapidly to temperature changes.

After obtaining two parameters of the time delays, the EDWHE model can be inverted through the linear least-square solution, thereby obtaining each estimate of the model coefficients, as shown in Figure 6. The first four estimated coefficients in Figures 6A–D are time-dependent terms representing the long-term plastic evolution. We know that plastic deformations accumulate gradually to significant magnitudes in a decaying way. Figures 6E, F indicates the magnitudes of the elastic expansion and contraction deformation of expansive soil. Figure 6E shows the deformations responding to rainfall infiltration, which are basically positive values, and have maximum values up to 0.12 mm/mm on some sections of the channel slopes. Figure 6F shows the temperature-related deformation coefficient, which illustrates a negative correlation with temperature in the channel slope and a significant positive correlation outside the channel in the urban area. Figure 6G shows the topographic discrepancies relative to the Copernicus DEM. The positive values mainly appear in urban areas, mostly caused by urban construction; there are also positive residual heights on the channel slope, which may also be caused by slope construction.

4.2 Deformation analysis

4.2.1 Spatial pattern of the InSAR deformation

Owing to the lack of knowledge about the study area's canal structure, we also collected 30 m resolution SRTM DEM of the corresponding area. We subtracted it from the sum of the Copernicus DEM and residual height (Figure 6G) to obtain the quasi-ground heights (Figure 7). Given the quasi-ground height results, we divided the channel in the study area into four main sections, as shown in Figure 7, delineated by the light gray dashed boxes "a-d".

The CSHC consists of completely excavated/filled or half-excavated and half-filled slopes, and a clear building distribution surrounding the channel can also be observed (Figure 7). Afterward, combined with the InSAR deformation results, the causes of specific deformation generation are discussed and analyzed. There are several clusters with positive coefficients of temperature-dependent deformation in urban regions (Figure 6F), corresponding to the significant positive height region in Figure 7. It is easy to infer that it is the result of the building's thermal expansion.

Subsequently, the InSAR products––the annual LOS displacement velocity and InSAR time series––could be derived. Here, we first describe the spatial characteristics of LOS displacement rates (Figure 8) and then discuss the InSAR time series. In these canal sections, the slope deformation does not distribute continuously or extensively but occurs in scattered small pieces, and the deformation rates are positive and negative, mainly fluctuating in the range of magnitude of 6.0–20 mm/year.
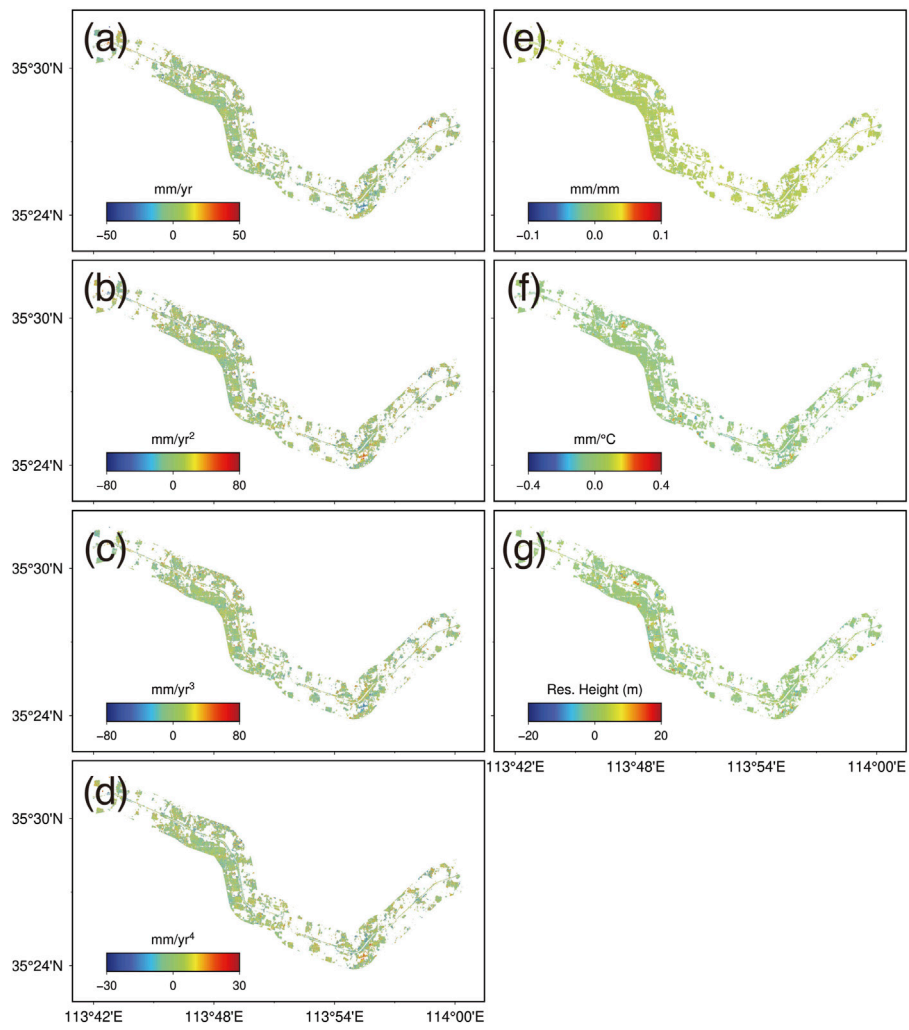
FIGURE 6
Estimated coefficients in the EDWHE model. Each subplot indicates the values of **(A)** α_1; **(B)** α_2; **(C)** α_3; **(D)** α_4; **(E)** β_1; **(F)** β_2; and **(G)** Δh.
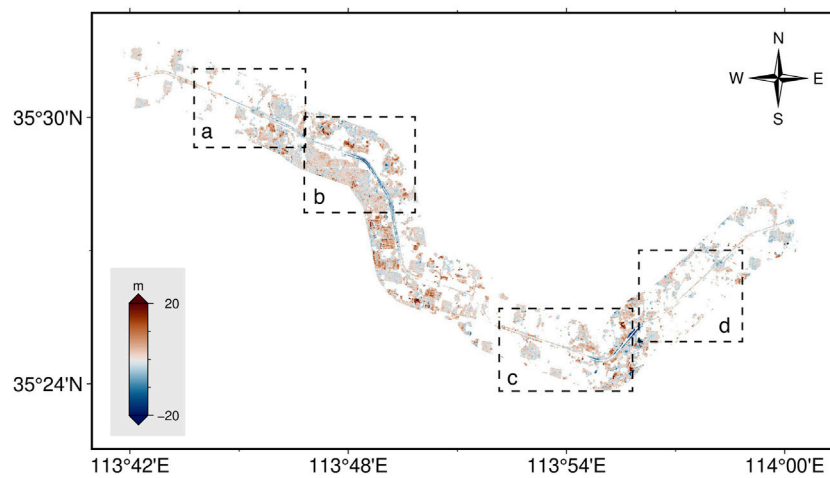

FIGURE 7
The difference between the 30 m SRTM dem and the sum of Copernicus dem and the estimated dem error Δh.
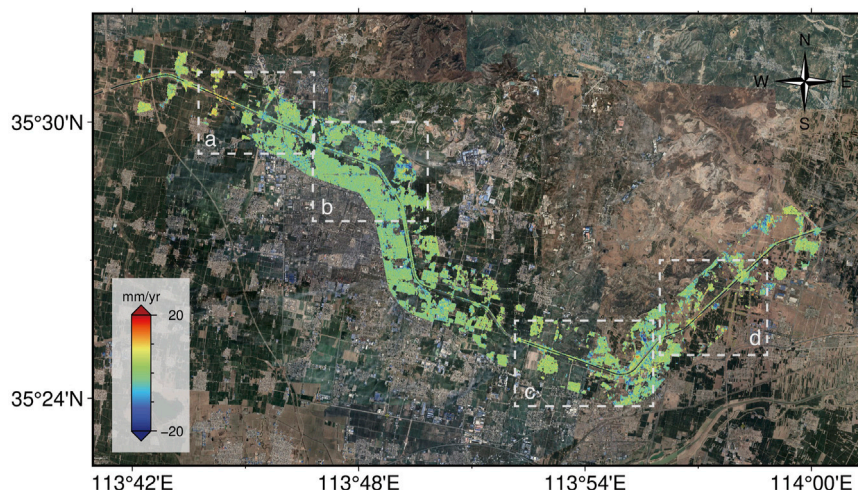
FIGURE 8
Annual LOS deformation rates. The dashed white boxes a–d indicate the local sections where the slopes with significant deformation are. The dashed black boxes a-d in Figure 7 delineate the same local regions.
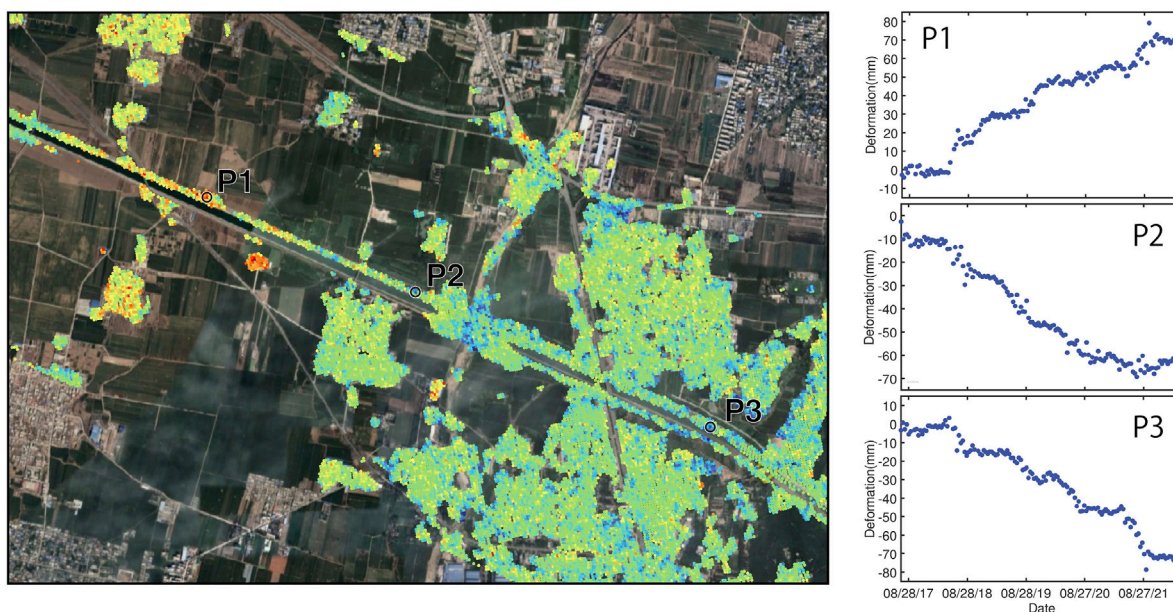

FIGURE 9
The magnified local region "a" denoted in Figure 7 and Figure 8, with the same colormap and scale as Figure 8.

The deformation magnitudes may result from heterogeneity in the ESSs of different formations and geological conditions. In addition, some of the causes of the observed deformation in the slope are possibly contributed to by slope maintenance or construction.

Furthermore, the four local regions "a-d" marked in Figure 8 are magnified separately to display where the time-series deformations on several feature points are plotted (Figures 9–12). According to the LOS deformation rates, we observed that the unstable slopes are small and distributed sparsely along

the channel. Then, we could understand that slope instability does not occur continuously or on a massive scale but rather in small and scattered areas, which significantly increases the challenge of slope monitoring and treating the unstable zones. The deformation time series of the unstable regions generally evolved exponentially and were accompanied by significant swelling and shrinkage (the featured points in Figures 9–12). We can note that there was a significant acceleration of the ESS displacements around 22 July 2021. It demonstrates that torrential rain on these days severely
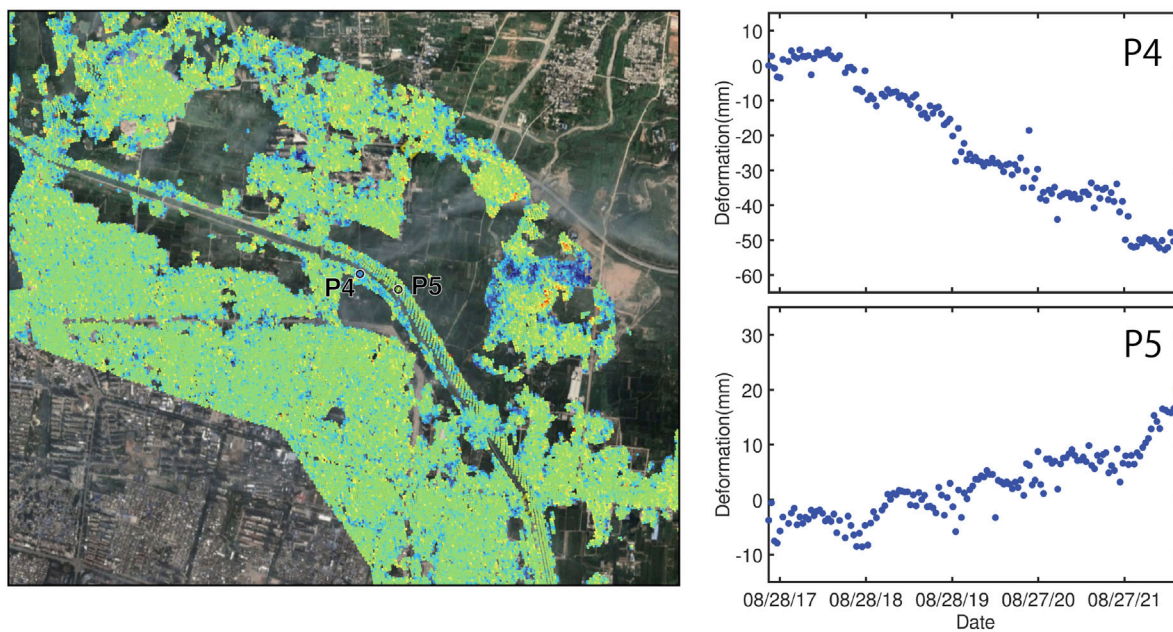
FIGURE 10
The magnified local region 'b" denoted in Figure 7 and Figure 8, with the same colormap and scale as Figure 8.
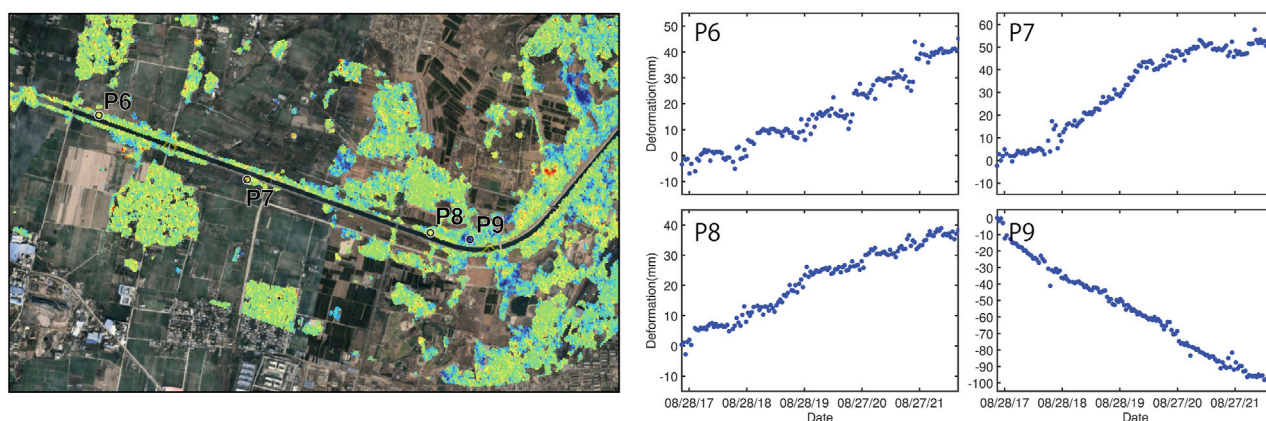

FIGURE 11
The magnified local region "c" denoted in Figure 7 and Figure 8, with the same colormap and scale as Figure 8.

impacted the stability of the ESS and facilitated their down-slope movements.

It is also intriguing that different locations on the channel slope exhibit diverse accumulation trends. Taking points P1 and P2 as an example, they are located at the canal section with the same slope direction, but their deformation trends are inverse, possibly because of the geometric structure of the slopes and the limitation of satellite SAR imagery. According to Figure 9, P2 is located at the filling part of a half-cut and half-fill slope, where settlement may occur at a significant magnitude, which turns out to be negative LOS deformation, and its temporally exponential evolution shown in Figure 9 proves this process. For other sub-regions, the feature points basically exhibit the elastoplastic characteristics as described

above. Except for P9 and P12, they (Figures 11, 12) are the points outside the canal slope, of which the displacements were caused by engineering construction.

Although the evolutions of time series with the deformation pattern specific to ESS were captured, the magnitudes of displacements seem to differ among sub-regions "a-d" of Figures 9–12. Specifically, the final accumulated LOS displacements of those featured points in sub-region "b, c" (except for P9) were generally less than those of others, i.e., sub-region "a, d", approximately 20 mm. It is presumable that the direction of the canal slope extending and the viewing mode of the SAR satellite causes this phenomenon, as a result of the deformation pattern of the downslope slide in the ESS; the LOS displacements in this case
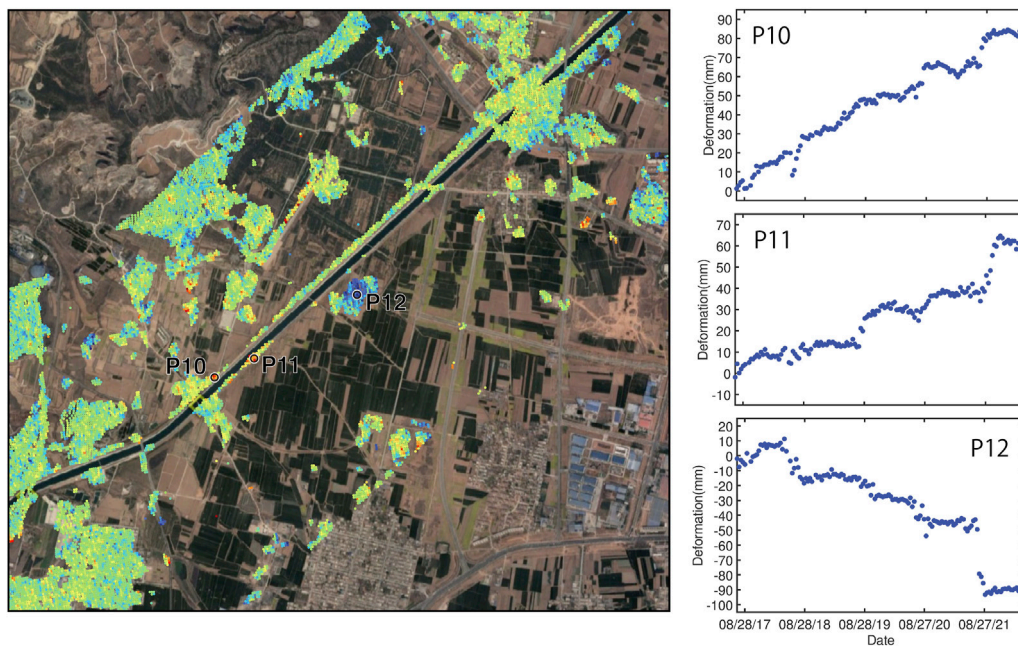
FIGURE 12
The magnified local region "d" denoted in Figure 7 and Figure 8, with the same colormap and scale as Figure 8.

will become larger at a slope that extends non-west-east than at one along "west-east" where the slope movements are approximately in a south-north direction, i.e., sub-region "b, c" (Ng et al., 2003; Li et al., 2023). It is a pity that only a single source of SAR data was available, and therefore, we could not view the deformation pattern of the ESS from a two-dimensional or even three-dimensional perspective (Zheng et al., 2023).

4.2.2 Dynamic of the elastic deformation

Elastic swelling and shrinkage are the main incentives for the progressive landslide of the ESS (Ng et al., 2003; Dai et al., 2021; Li et al., 2023); therefore, further analysis of its evolving characteristics is necessary. Therefore, in this section, we decouple the ESS's deformation through the EDWHE model and then derive the elastic-plastic component. Here, the time series of elastic deformation corresponding to P2, P5, and P7 are analyzed as examples (Figure 13). Among them, the delay times of points P2, P5, and P7 corresponding to rainfall infiltration are 18, 2, and 153 days, respectively; the temperature-induced ones are 49, 3, and 6 days, respectively.

The elastic deformation is prone to obvious shrinkage deformation under the influence of high temperature every summer, corresponding to the green fitting lines in Figure 13 significantly evolving downward during that period. Under the temperature change, the elastic contraction presented periodic changes on a long-term scale. However, summer also corresponds with a rainy season; therefore, it can be observed that the elastic deformation appears to uplift mid-year in some years with heavy rainfall. In the extraordinary rainstorm that occurred in July 2021, significant swelling can be observed as a result of a large amount of rainfall infiltration, which is also the reason for the significant acceleration of plastic deformation during

this period. In addition, we find that, for P7, the response of the soil shrinkage to temperature is not obvious; by contrast, it responds greatly to rainfall events and therefore it mainly shows expansion deformation in summer. This may be attributed to the different geological properties of P7.

The elastic deformation mentioned above is the process of swelling and shrinkage coupling, which results in uplift or settlement, as analyzed previously, mainly depending on geological and meteorological conditions. Under monsoon effects, the frequent swelling and shrinkage provide more chances to weaken slope strength and accelerate slope instability (Ng et al., 2003; Bao, 2004).

4.3 Active zone depth

Owing to the lack of ground measurement data in the study area, the necessary parameters in Equation (8) were determined empirically by the moisture diffusion coefficient $\hat{\alpha} = 10^{-7} m^2/s$ and suction cycle frequency $n = 2$. Here, to focus on the AZD distribution pattern of the ESS in the CSHC, the region outside the channel was cut out, and the retrieval of the AZD was then completed, which is shown in Figure 14. The most active zones are in shallow layers of expansive soil, and the other part of them extends to greater depths, up to 4 m. It does reflect the spatial distribution of the AZD at different locations. Additionally, we could see that the AZDs on the bridges across the channel are generally close to zero, which means there is no active zone under the bridges. Furthermore, most of the AZDs are uniform and continuous along the canal sections (e.g., downstream of the channel in Figures 14C, D). In fact, in the shallow active zone in the canal slope, those AZDs close to 0 demonstrate the effectiveness of the waterproof measure on the ESS
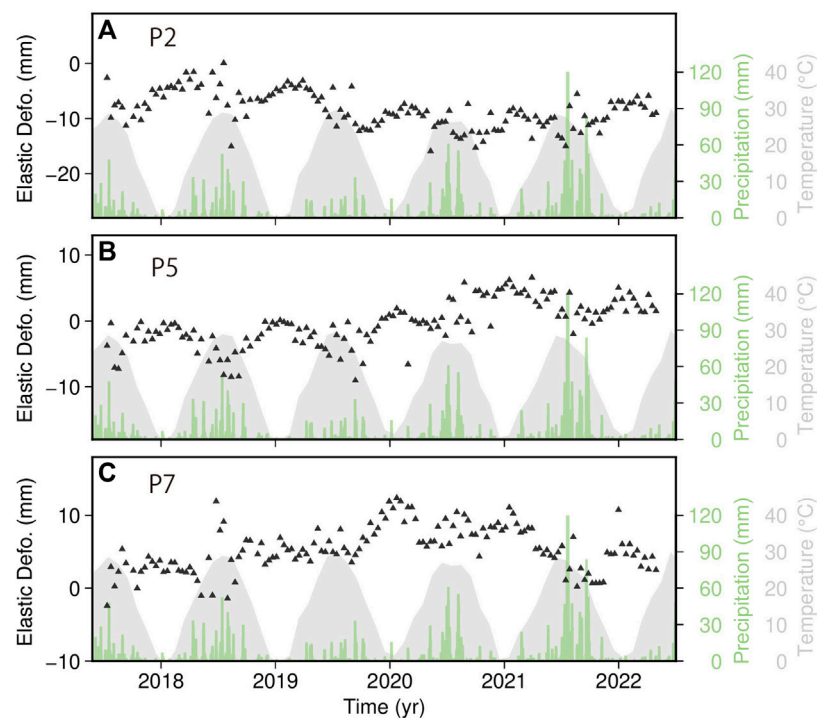
FIGURE 13
Evolutions of the elastic swelling-shrinkage deformations. Three elastic deformation time series are located at feature points **(A)** P2, **(B)** P5, and **(C)** P7. The black triangles indicate the elastic deformation of the expansive soil, which is then fitted by the solid green lines. The light green and gray shadows are the daily precipitation and monthly temperature.

that prevents moisture or rainwater from permeating deeper. However, there are discrete and abnormal values among the uniform AZDs in some sections (e.g., Figures 14A, B). It may be the reason that the construction and maintenance of the ESS during the monitoring period brought in a different deformation pattern unrecognizable to the EDWHE model, which can probably lead to the overestimated time lag and then the abnormally high value of the AZD in some locations.

Although using the time-lag approach to calculate AZD has been evaluated in the geotechnical field and has demonstrated its effectiveness, the lack of ground data makes it the only choice for determining the diffusion coefficient α empirically by Tu and Vanapalli (2016) and stops further quantitative analysis of AZD retrieval based on the InSAR results. Therefore, in the future, it will be necessary to use *in situ*-measured AZD to verify the efficiency of the InSAR-based method of retrieving AZD.

5 Conclusion

In this study, we collected 144 Sentinel SAR data between July 2017 to May 2022 to study the behavior of expansive soil in the Huixian section of the MR-SNWDP to provide a further understanding of ESS displacement and investigate the impact of torrential rainstorms on the stability of the ESS, consequently supporting the protective measure for geohazards in expansive

soil in the MR-SNWDP. To this end, the EDWHE model was applied to interpret the expansive soil's elastoplastic deformation. Except for deriving the deformation results by solving the model, the time delays responsible for rainfall and temperature were estimated simultaneously, and the rainfall-induced delay was used for subsequent AZD retrieval using the time-lag approach.

According to the estimated time delays, the expansive soil deformation responses are longer for rainfall infiltration than for temperature change. As revealed by the InSAR results, the unstable zones are small and distributed on the channel slope in the study area, where the LOS deformation rates are generally no more than the absolute values of 20 mm/year. The displacement time series on some feature points temporally accumulate with significant seasonal swelling and shrinkage. The extreme torrential rains on 22 July 2021, in Huixian City led to the significant displacement acceleration of the ESS. Owing to the slope aspects and geometric structure in different locations, the magnitudes and evolving trends of the ESS's LOS displacements may be different. Additionally, the elastic deformations are derived through the model. We find there is significant coupled swelling and shrinkage in the rainy/hot season, and the elastic deformation presenting uplift or settlement mainly depends on geological and meteorological conditions.

The depths of the active zone in the study area were obtained through the InSAR-based lag-time approach, which illustrated their spatial distribution pattern with high resolution. Even though we
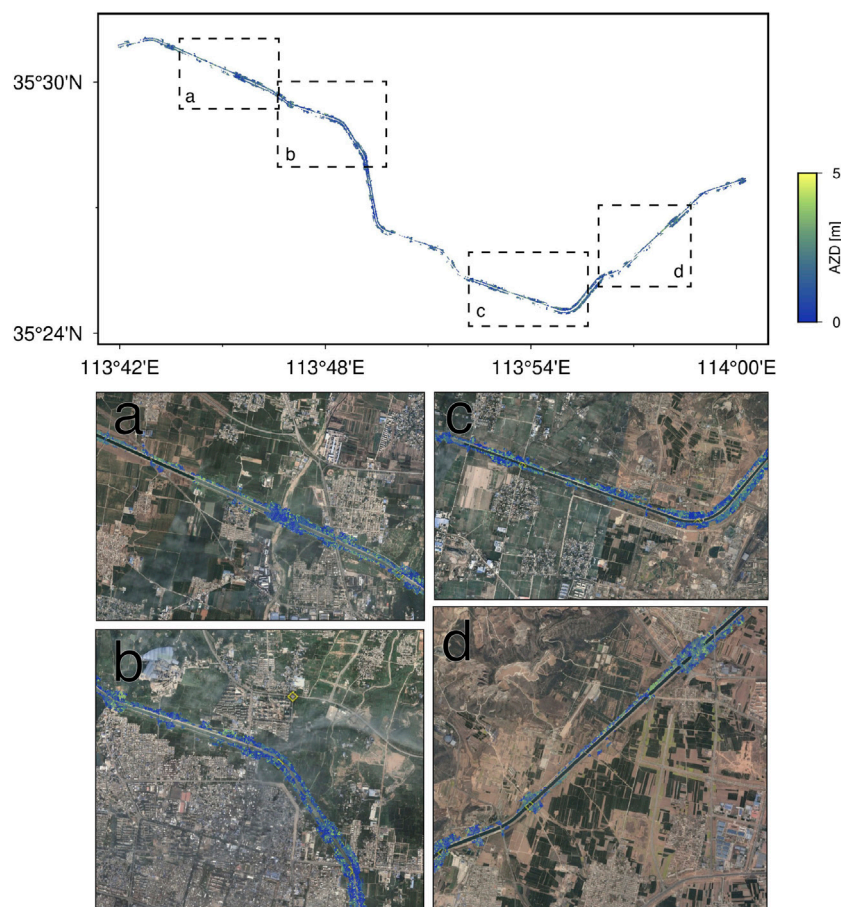
FIGURE 14
The Active Zone Depth (AZD) results along the channel.

could not further quantify the accuracy of the retrieved AZD because of the limited available ground data, it does provide the potential to support the protective measures for the unstable ESS in the MR-SNWDP.

Nevertheless, the studies carried out in this paper investigated the behavior of the ESS from a macroscopic perspective using InSAR and can offer a better understanding of the prevention of expansive soil geohazards, which is significant for the safety of the MR-SNWDP.

Data availability statement

The original contributions presented in the study are included in the article/Supplementary Material, further inquiries can be directed to the corresponding author.

Author contributions

ZJ: Validation, Writing–original draft, Writing–review and editing. ZW: Funding acquisition, Resources, Validation, Writing–review and editing. ZL, Conceptualization, Formal analysis, Investigation, Methodology, Software, Validation,

Visualization, Writing–original draft, Writing–review and editing. JH: Conceptualization, Funding acquisition, Investigation, Project administration, Supervision, Validation, Writing–original draft, Writing–review and editing. YW: Data curation, Investigation, Resources, Validation, Writing–review and editing. LO: Data curation, Investigation, Validation, Writing–review and editing. TZ: Resources, Validation, Writing–review and editing.

Funding

Acknowledgments

(https://www.asf.alaska.edu/sentinel/accessed on 24 March 2023). The Copernicus DEM used in this study can be downloaded from the Nevada Geodetic Laboratory (https://www.opentopography.org accessed on 24 March 2023).

Conflict of interest

Authors ZW and TZ were employed by State Grid Ji'an Electric Power Supply Company.

The remaining authors declare that the research was conducted in the absence of any commercial or financial relationships that could be construed as a potential conflict of interest.

Publisher's note

All claims expressed in this article are solely those of the authors and do not necessarily represent those of their affiliated organizations, or those of the publisher, the editors and the reviewers. Any product that may be evaluated in this article, or claim that may be made by its manufacturer, is not guaranteed or endorsed by the publisher.

Supplementary material

The Supplementary Material for this article can be found online at: https://www.frontiersin.org/articles/10.3389/fenvs.2023.1287128/full#supplementary-material

References

Aubeny, C., and Long, X. (2007). Moisture diffusion in shallow clay masses. *J. Geotechnical Geoenvironmental Eng.* 133, 1241–1248. doi:10.1061/(asce)1090-0241(2007)133:10(1241)

Bao, C. (2004). Behavior of unsaturated soil and stability of expansive soil slope. *Chin. J. Geotechnical Eng.*, 1–15. doi:10.3321/j.issn:1000-4548.2004.01.001

Bekaert, D. P. S., Hooper, A., and Wright, T. J. (2015). A spatially variable power law tropospheric correction technique for InSAR data. *J. Geophys. Res. Solid Earth* 120, 1345–1356. doi:10.1002/2014JB011558

Bonì, R., Bosino, A., Meisina, C., Novellino, A., Bateson, L., and McCormack, H. (2018). A methodology to detect and characterize uplift phenomena in urban areas using sentinel-1 data. *Remote Sens.* 10, 607. doi:10.3390/rs10040607

Chaussard, E., Wdowinski, S., Cabral-Cano, E., and Amelung, F. (2014). Land subsidence in central Mexico detected by ALOS InSAR time-series. *Remote Sens. Environ.* 140, 94–106. doi:10.1016/j.rse.2013.08.038

Cohen-Waeber, J., Bürgmann, R., Chaussard, E., Giannico, C., and Ferretti, A. (2023). Spatiotemporal patterns of precipitation-modulated landslide deformation from independent component analysis of InSAR time series. *Geophys. Res. Lett.* 45, 1878–1887. doi:10.1002/2017gl075950

Cook, M. E., Brook, M. S., Hamling, I. J., Cave, M., Tunnicliffe, J. F., and Holley, R. (2023). Investigating slow-moving shallow soil landslides using Sentinel-1 InSAR data in Gisborne, New Zealand. *Landslides* 20, 427–446. doi:10.1007/s10346-022-01982-9

Costantini, M., and Rosen, P. A. (1999). "A generalized phase unwrapping approach for sparse data," in IEEE 1999 International Geoscience and Remote Sensing Symposium. IGARSS'99 (Cat. No.99CH36293), Hamburg, Germany, June, 1999, 267–269. doi:10.1109/IGARSS.1999.773467

Dai, Z., Zhang, C., Wang, L., Fu, Y., and Zhang, Y. (2021). Interpreting the influence of rainfall and reservoir water level on a large-scale expansive soil landslide in the Danjiangkou Reservoir region, China. *Eng. Geol.* 288, 106110. doi:10.1016/j.enggeo.2021.106110

Delbridge, B. G., Bürgmann, R., Fielding, E., Hensley, S., and Schulz, W. H. (2016). Three-dimensional surface deformation derived from airborne interferometric UAVSAR: application to the Slumgullion Landslide. *J. Geophys. Res. Solid Earth* 121, 3951–3977. doi:10.1002/2015JB012559

Dong, J., Guo, S., Wang, N., Zhang, L., Ge, D., Liao, M., et al. (2023). Tri-decadal evolution of land subsidence in the Beijing Plain revealed by multi-epoch satellite InSAR observations. *Remote Sens. Environ.* 286, 113446. doi:10.1016/j.rse.2022.113446

Dong, J., Lai, S., Wang, N., Wang, Y., Zhang, L., and Liao, M. (2021). Multi-scale deformation monitoring with sentinel-1 InSAR analyses along the middle route of the Southsouth-north water diversion project in China. *Int. J. Appl. Earth Observation Geoinformation* 100, 102324. doi:10.1016/j.jag.2021.102324

Goldstein, R. M., and Werner, C. L. (1998). Radar interferogram filtering for geophysical applications. *Geophys. Res. Lett.* 25, 4035–4038. doi:10.1029/1998GL900033

Hu, X., Bürgmann, R., Schulz, W. H., and Fielding, E. J. (2020). Four-dimensional surface motions of the Slumgullion landslide and quantification of hydrometeorological forcing. *Nat. Commun.* 11, 2792–2799. doi:10.1038/s41467-020-16617-7

Huang, Z., Shi, H., Zhang, W., Ma, S., Gao, F., and Ma, M. (2022). Expansive soil embankment filling and cutting treatment Technology: a systematic review. *Adv. Mater. Sci. Eng.* 2022, 1–20. doi:10.1155/2022/4045620

Jiang, J., and Lohman, R. B. (2021). Coherence-guided InSAR deformation analysis in the presence of ongoing land surface changes in the Imperial Valley, California. *Remote Sens. Environ.* 253, 112160. doi:10.1016/j.rse.2020.112160

Lan, H., Zhao, X., Macciotta, R., Peng, J., Li, L., Wu, Y., et al. (2021). The cyclic expansion and contraction characteristics of a loess slope and implications for slope stability. *Sci. Rep.* 11, 2250. doi:10.1038/s41598-021-81821-4

Li, Z., Cao, Y., Wei, J., Duan, M., Wu, L., Hou, J., et al. (2019). Time-series InSAR ground deformation monitoring: atmospheric delay modeling and estimating. *Earth-Science Rev.* 192, 258–284. doi:10.1016/j.earscirev.2019.03.008

Li, Z., Hu, J., Zhang, X., Zheng, W., Wu, W., Chen, Y., et al. (2023). Characterization of elastoplastic behavior and retrieval of active zone depth for expansive soil slopes in the middle-route channel head of the South-to-North Water Diversion Project, China, using InSAR time series. *Remote Sens. Environ.* 295, 113666. doi:10.1016/j.rse.2023.113666

Liang, H., Zhang, L., Ding, X., Lu, Z., and Li, X. (2019). Toward mitigating stratified tropospheric delays in multitemporal InSAR: a quadtree aided joint model. *IEEE Trans. Geoscience Remote Sens.* 57, 291–303. doi:10.1109/TGRS.2018.2853706

Miller, M. M., Shirzaei, M., and Argus, D. (2017). Aquifer mechanical properties and decelerated compaction in tucson, Arizona: tucson subsidence and aquifer properties. *J. Geophys. Res. Solid Earth* 122, 8402–8416. doi:10.1002/2017JB014531

Mitchell, P. W. (1980). The structural analysis of footings on expansive soil. In (ASCE). Available at: https://cedb.asce.org/CEDBsearch/record.jsp?dockey=0031270 (Accessed June 23, 2022).

Murray, K. D., and Lohman, R. B. (2018). Short-lived pause in Central California subsidence after heavy winter precipitation of 2017. *Sci. Adv.* 4, eaar8144. doi:10.1126/sciadv.aar8144

Ng, C. W. W., Zhan, L. T., Bao, C. G., Fredlund, D. G., and Gong, B. W. (2003). Performance of an unsaturated expansive soil slope subjected to artificial rainfall infiltration. *Géotechnique* 53, 143–157. doi:10.1680/geot.2003.53.2.143

Office of the South-to-North Water Diversion Project Construction Committee, State Council, and PRC (2016). The South-to-North Water diversion project. *Engineering* 2, 265–267. doi:10.1016/J.ENG.2016.03.022

Özer, I. E., Rikkert, S. J. H., van Leijen, F. J., Jonkman, S. N., and Hanssen, R. F. (2019). Sub-seasonal levee deformation observed using satellite radar interferometry to enhance flood protection. *Sci. Rep.* 9, 2646–2710. doi:10.1038/s41598-019-39474-x

Qi, S., and Vanapalli, S. K. (2016). Influence of swelling behavior on the stability of an infinite unsaturated expansive soil slope. *Comput. Geotechnics* 76, 154–169. doi:10.1016/j.compgeo.2016.02.018

Rodriguez, E., and Martin, J. M. (1992). Theory and design of interferometric synthetic aperture radars. *IEE Proc. F (Radar Signal Process.* 139, 147–159. doi:10.1049/ip-f-2.1992.0018

Shi, B., Jiang, H., Liu, Z., and Fang, H. Y. (2002). Engineering geological characteristics of expansive soils in China. *Eng. Geol.* 67, 63–71. doi:10.1016/S0013-7952(02)00145-X

Ting, L., Chaosheng, T., Dan, X. U., Yunsheng, L. I., Yan, Z., Kan, W., et al. (2018). Advance on the engineering geological characteristics of expansive soil. *gcdzxb* 26, 112–128. doi:10.13544/j.cnki.jeg.2018.01.013

Tu, H., and Vanapalli, S. K. (2016). Prediction of the variation of swelling pressure and one-dimensional heave of expansive soils with respect to suction using the soil-water retention curve as a tool. *Can. Geotech. J.* 53, 1213–1234. doi:10.1139/cgj-2015-0222

Vallone, P., Giammarinaro, M. S., Crosetto, M., Agudo, M., and Biescas, E. (2008). Ground motion phenomena in Caltanissetta (Italy) investigated by InSAR and geological data integration. *Eng. Geol.* 98, 144–155. doi:10.1016/j.enggeo.2008.02.004

Wang, G., and Wei, X. (2014). Modeling swelling–shrinkage behavior of compacted expansive soils during wetting–drying cycles. *Can. Geotechnical J.* 52, 783–794. doi:10.1139/cgj-2014-0059

Xiong, S., Deng, Z., Zhang, B., Wang, C., Qin, X., and Li, Q. (2023). Deformation evaluation of the SouthSouth-to-North water diversion project (SNWDP) central route over handan in hebei, China, based on sentinel-1A, radarsat-2, and TerraSAR-X datasets. *Remote Sens.* 15, 3516. doi:10.3390/rs15143516

Xu, D., Liu, H., Zhang, Y., Li, Y., and Chen, Y. (2019). Study on application of PS-InSAR technique in safety monitoring of expansive soil zone in South-to-North water diversion middle route project in huixian, henan Province. *Geomatics Spatial Inf. Technol.* 42, 31–34.

Yang, H.-P., Zhang, R., and Zheng, J.-L. (2006). Variation of deformation and strength of expansive soil during cyclic wetting and drying under loading condition. 28, 1936–1941.

Yue, Er, and Veenstra, J. N. (2018). Prediction of active zone depth in Oklahoma using soil matric suction. *J. Geoengin.* 13. doi:10.6310/jog.201803_13(1).3

Yunjun, Z., Fattahi, H., and Amelung, F. (2019). Small baseline InSAR time series analysis: unwrapping error correction and noise reduction. *Comput. Geosciences* 133, 104331. doi:10.1016/j.cageo.2019.104331

Zebker, H. (2021). Accuracy of a model-free algorithm for temporal InSAR tropospheric correction. *Remote Sens.* 13, 409. doi:10.3390/rs13030409

Zhan, L., Chen, P., and Ng, C. W. W. (2007). Effect of suction change on water content and total volume of an expansive clay. *J. Zhejiang Univ. - Sci. A* 8, 699–706. doi:10.1631/jzus.2007.A0699

Zhang, S., Si, J., Niu, Y., Zhu, W., Fan, Q., Hu, X., et al. (2022). Surface deformation of expansive soil at ankang airport, China, revealed by InSAR observations. *Remote Sens.* 14, 2217. doi:10.3390/rs14092217

Zhang, Y., Tian, F., Li, Y., and Liu, H. (2021). Application of time series InSAR to deformation monitoring in central line project of South-to-North water transfer. *J. Yangtze River Sci. Res. Inst.* 38, 72–77.

Zhao, R., Li, Z., Feng, G., Wang, Q., and Hu, J. (2016). Monitoring surface deformation over permafrost with an improved SBAS-InSAR algorithm: with emphasis on climatic factors modeling. *Remote Sens. Environ.* 184, 276–287. doi:10.1016/j.rse.2016.07.019

Zheng, W., Hu, J., Lu, Z., Hu, X., Sun, Q., Liu, J., et al. (2023). Enhanced kinematic inversion of 3-D displacements, geometry, and hydraulic properties of a north-south slow-moving landslide in three gorges reservoir. *J. Geophys. Research-Solid Earth* 128, e2022JB026232. doi:10.1029/2022JB026232

Zongjun, P. a. N., Yongli, X. I. E., Xiaohua, Y., and Zhifeng, L. I. (2006). Depth identification of the active and cracking zones in expansive soils from *in-situ* suction measurement. *gcdzxb* 14, 206–211.